Oscillation Mechanism and Mitigation of MMC-HVDC Based on Bifurcation Theory for Wind Farm Integration

YONGJIN YU[ID], **XUEZHEN CHENG**[ID], **CHAO ZHANG**[ID], **AND XINGQUAN JI**[ID]

College of Electrical Engineering and Automation, Shandong University of Science and Technology, Qingdao 266590, China

Corresponding author: Xuezhen Cheng (chenxz_sdust@163.com)

ABSTRACT Modular multilevel converter based highvoltage DC transmission (MMC-HVDC) technology has become a feasible approach from grid integration of large wind farms. As oscillations has been reported on certain number of MMC-HVDC projects with wind power, the mechanism and analytical methods are urgent issues for studying. The current commonly used modeling methods cannot meet the characteristics of MMC topology due to the complex pulse mode shown in a switching period. Therefore, a new method is proposed to effectively solve the stroboscopic mapping modeling problem of multilevel converters. On the basis of traditional proportional resonant (PR) control, a time-delay feedback control (TDFC) loop is added to effectively suppress the current oscillation. Taking the 21 level MMC topology as an example, the discrete model is obtained by the method of switch state traversal, and the correctness of the theoretical analysis and the proposed strategy of oscillation current suppression is verified by simulation.

INDEX TERMS Modular multilevel converter, oscillations, time-delay feedback control, stroboscopic map.

I. INTRODUCTION

MMC- HVDC has attracted attention due to its advantages such as low output voltage harmonic content, flexible structure and favorable expansibility [1]–[3]. The transmission of the large-scale centrally developed wind power through MMC- HVDC has become the trend of technique development, and several projects have been put into operation or under planning and construction [4]–[6]. But with the continuous increase of the installed proportion of wind power in some areas, the connected synchronous power grid is gradually weakened, the stability characteristics of the power system have profoundly changed, and the broadband oscillation phenomenon of large-scale integrated wind power occurs frequently, which critically affects the security and stability of power grid operation [7]–[10].

A number of wind farms have undergone oscillation during the commissioning or operation stage through the MMC-HVDC transmission project [11], [12]. For example,

The associate editor coordinating the review of this manuscript and approving it for publication was Huanqing Wang.

in the North Sea Borwin1 project in Germany, an intermediate frequency oscillation of about 290 Hz occurred [13], [14] and the filter capacitors of HVDC offshore platform burned out, which caused the system to be out of service for half a year. In order to avoid the above-mentioned oscillation phenomenon in the project, it is necessary to analyze the oscillation mechanism of the wind farms output system through MMC-HVDC. The broadband time-varying characteristics of oscillation is extremely demanding for its suppression strategy and parameter robustness, and it is a key problem to be solved in oscillations suppression. In terms of oscillations suppression, research that has been carried out focuses on three aspects: optimization of converter control parameters, supplementary damping control of wind turbine converters, and suppression strategies based on HVDC technology [15], [16].

Oscillations of the wind farms output system through MMC-HVDC is different from that caused by traditional series capacitor compensation and fan shaft system torsion. When considering the DC voltage dynamics, the oscillation mode of the wind farms output system through MMC-HVDC

is caused by the grid side converter controller, and mainly affected by the control system parameters, control mode and grid connection mode of the converter. The traditional methods of processing the oscillation signal are mostly based on the steady-state, but the oscillations signal belongs to the wide-band transient component [17]. So the advanced digital signal processing method is needed to provide the basis for the monitoring and diagnosis of oscillations.

Chaos refers to the process similar to random in the deterministic system, which is the existence form of nonlinear system between certainty and randomness. Chaos is the solution of the inherent randomness of the deterministic nonlinear system. Bifurcation is mainly used to study a measure of local and global similarity of waveforms. Oscillations of the wind farms output system through MMC-HVDC is a non-stationary random process, and its state characteristics fully meet the principle calculation of chaos and bifurcation. Therefore, this paper mainly studies the bifurcation and chaos in MMC-HVDC used for the controller parameters design of the converter, in order to suppress the oscillation of the wind farms output system through MMC-HVDC.

Currently, the research of MMC topology mainly utilizes the state spaces average model to analyze the stable region, or builds a specific discrete model for the specific state of the converter, and conducts simulation analysis step by step. However, neither of these two methods can properly seek solution to the problem of stability domain of the converter, in which the state spaces average model has a large error when the switching frequency is low, while the step-by-step analysis method can only get the step-by-step time-domain solution of the converter, but not the stability domain. To analyze the bifurcation and chaos of MMC, it is necessary to establish a corresponding precise discrete model. However, common modeling methods are difficult to be applied since the number of levels varies in each sampling period due to the complex pulse mode of MMC topology. Therefore, this paper presents a virtual traversing modelling method, which effectively solves the problem of difficult modeling due to the complexity of pulse mode in a single period.

The proposed method has three major novelties: (i) the chaos method based on transient data is used to analyze the oscillation of MMC, instead of the traditional fault analysis based on steady-state data; (ii) the virtual traversing model is established to analyze the bifurcation and chaos of MMC; (iii) the bifurcation method is used to analyze the control parameters selection and the controller is designed, to suppress the chaos of power grid and reduce the influence of oscillation.

The rest of this paper is organized as follows. Section II describes the model of MMC-HVDC for wind farm integration. Section III establishes the discrete mapping model to analyze the chaotic characteristics of oscillation. Section V proposes the bifurcation method to analyze the characteristics of parameters and design the controller. Section VI provides industrial examples to illustrate the obtained results. Some concluding remarks are given in Section VII.
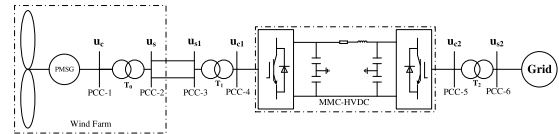

FIGURE 1. Topology of MMC-HVDC for Wind Farm Integration.

II. MODEL OF MMC-HVDC FOR WIND FARM INTEGRATION

Fig. 1 shows the topological structure of the output system of the wind farm through MMC-HVDC. The wind farm consists of full-power wind turbines and utilizes full-power back-to-back converters, with a generator terminal voltage of 690 V, which is connected to the 35 kV collector line through the generator terminal transformer, and the outlet of the wind farm is connected to MMC-HVDC system via a booster transformer of 35/110 kV. MMC-HVDC system is composed of wind farm-side MMC station, grid-side MMC station and DC transmission line. Under normal operation, the wind farm-side MMC converter station is responsible for controlling the amplitude and frequency of AC voltage at the point of common coupling (PCC-1) with the wind farm to provide stable AC power; the grid-side MMC station is in charge of controlling the stability of DC transmission voltage and providing a certain amount of reactive power to AC grid.

For MMC, each sub-module (SM) in the bridge arm can be individually controlled in input or removal to dominate the voltage value of the bridge arm, so each bridge arm is equivalent to a controllable voltage source. The equivalent circuit diagram of the MMC-side system is shown in Fig. 2.

The topology of one SM is shown in Fig. 3, which mainly includes two IGBTs, two antiparallel diodes and capacitors. u_{sm} is the voltage at both ends of SM, i_{sm} is the current flowing into the SM, A and B are the connection ports where the SM is connected in series to the main circuit topology, while MMC is an electric voltage of DC transmission line supported by the capacitor voltage of each SM. According to the combination of different switching states and current directions of the two IGBTs, SM can be divided into three operation states and six operation modes.

Stroboscopic mapping model is widely used in the study of chaos in power converters. The clock period T_s is used as the sampling interval, and the state variable at the nT_s time is utilized to represent the state variable at the $(n + 1)T_s$ time, therefore getting the stroboscopic mapping model of the system. According to the traditional method of discrete modeling on MMC module, its mathematical model is shown in equation:

$$\frac{\mathrm{d}i_{sp}}{\mathrm{d}t} = -\frac{R}{L}i_{sp} + \frac{u}{L}, \quad u \in \{U_{dc}, -U_{dc}\}, \ p = a, b, c \quad (1)$$

where i_{sp} is the source current, R and L are the load resistance and inductance, and U_{dc} is the DC voltage source voltage.

According to equation (1), let the initial condition of the current be i_n, the duty cycle be d_n, and the value of the current at the end of the previous operation mode is the solution of
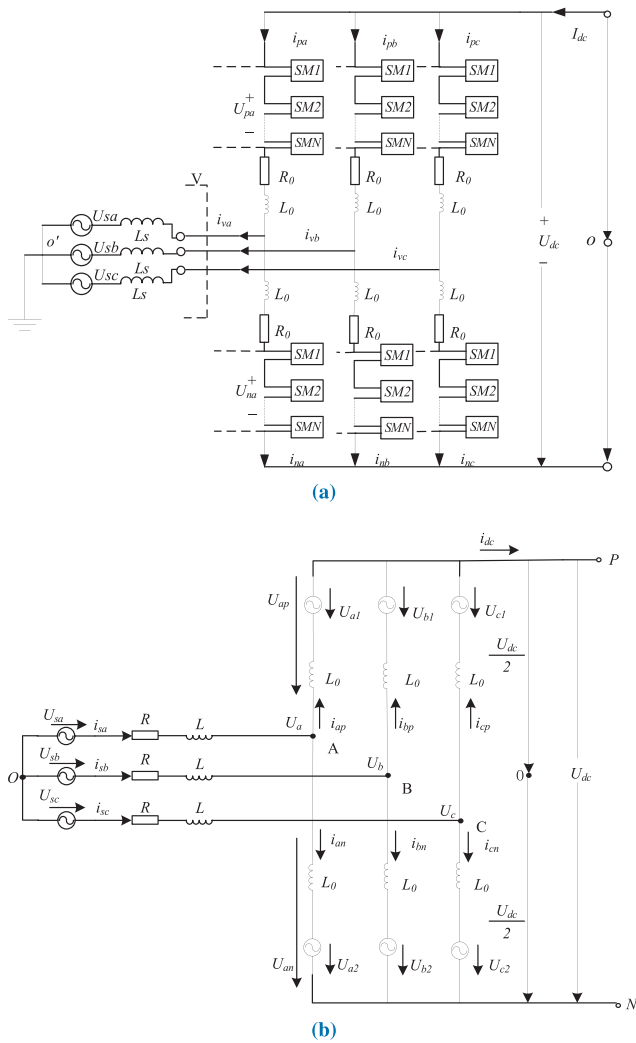
(a)

(b)

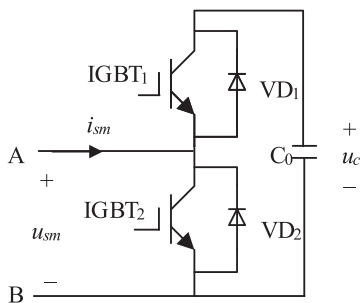**FIGURE 2.** Equivalent circuit diagram of MMC.

FIGURE 3. Topology diagram of SM.

the differential equation $\frac{di_{sp}}{dt} = -\frac{R}{L}i_{sp} + \frac{U_{dc}}{L}$, that is,

$$y = \alpha + (i_{n,sp} - \alpha)e^{-d_n T_s/\tau}, \qquad (2)$$

where, $\alpha = U_{dc}/R$, $\tau = L/R$. After switching the operation mode, the evolution mode of the current is determined by equation:

$$\frac{di_{sp}}{dt} = -\frac{R}{L}i_{sp} + \frac{-U_{dc}}{L} \qquad (3)$$

By substituting the final value y of the previous operation mode as the initial value and considering the actuation duration as $(1 - d_n)T_s$, the discrete mapping model of the MMC unit can be derived, as shown in equation (4).

$$i_{n+1,sp} = (i_{n,sp} - \alpha)e^{-\frac{T_s}{\tau}} + 2\alpha e^{\frac{-(1-d_n)T_s}{\tau}} - \alpha \qquad (4)$$

A mathematical model for the 21 levels MMC is composed of 21 equations, as shown in equation (5).

$$\frac{di_{sp}}{dt} = -\frac{R}{L}i_{sp} + \frac{\delta U_{dc}}{L}, \quad \delta \in \{n, 0, -n\}, \ n = 1, 2, \dots, 10 \qquad (5)$$

where δ is the coefficient of the electrical level.

The in-phase disposition (IPD) amplitude shifts carrier modulation method is adopted for the MMC, but it is difficult to determine the system discrete model in a sampling period due to the different effect levels in each period. A compromise method is to set up 21 discrete equations for 21 levels respectively, but it is impossible to distinguish the system stability in a global sense. Therefore, considering the characteristics of SPWM modulation, this paper combines the above 21 levels in pairs according to the modulation law, extends them into forty levels and establishes a unified discrete model with global significance.

There are twenty toggle states of the output level U in one switching period T_s, which correspond to the comparison of the channel carriers and the modulated wave V^*. Different modulation amplitude values correspond to diverse output level. For example, the output level is $(2U_{dc}, U_{dc})$ when the modulation amplitude value $V^* \in (1, 2)$. Suppose that the action time of level $2U_{dc}$ and level U_{dc} is t_1 and t_2 respectively, where the values of t_1 and t_2 are determined by the duty circle d, and $t_1 + t_2 = T_s$. According to this setting, when the modulated wave $V^* \in (0, 1)$, the output level is $(U_{dc}, 0)$ while the action time is t_3 and t_4 respectively, and $t_3 + t_4 = T_s$; when the modulated wave $V^* \in (-1, 0)$, the output level is $(0, -U_{dc})$ with an action time of t_5 and t_6 respectively, and $t_5 + t_6 = T_s$; when the modulated wave $V^* \in (-2, -1)$, the output level is $(-U_{dc}, -2U_{dc})$ and the action time is t_7 and t_8 respectively, with $t_7 + t_8 = T_s$.

There is only one toggle state of output level in a specific switching period. For example, when the modulated wave $V^* = 1.5$, the output level merely switches between $(2U_{dc}, U_{dc})$. Although it is previously considered that only the values of t_1 and t_2 exist, the proposed method holds that $t_3 \sim t_{40}$ also exists, with the value of 0. Taking all possible level toggle states into consideration, it is suggested that each level has taken effect in the same switching period, although the action time of some levels is 0. The equation (3) is extended to forty differential equations, as shown in equation (6).

$$\frac{di_{sp}}{dt} = -\frac{R}{L}i_{sp} + \frac{\delta U_{dc}}{L}, \ \delta \in \{10\ 9\} \cup \{9\ 8\} \cup \dots \cup \{-9\ -10\} \qquad (6)$$

where, the coefficient of level δ is assumed to take forty values from the above equation in turn within the same sampling period. In fact, only two values in the above equation can be taken in the same sampling period.

III. DISCRETE MATHEMATICAL MODEL OF MMC

In order to seek solutions of the forty differential equations in equation (6), a standard differential equation and its solution are given first, as shown in equation (7).

$$\frac{dy}{dt} = ay + b, \quad y = -\frac{b}{a} + Ce^{at} \qquad (7)$$

Equation (7) can be repeatedly applied in the subsequent process of solving differential equations, and only the coefficient C of the solution needs to be determined.

If δ in equation (6) is $\delta_1, \delta_2, \ldots, \delta_{40}$ respectively, the forty differential equations in equation (4) can be represented by one equation, as shown in equation (6).

$$\frac{di_{sp}}{dt} = -\frac{R}{L}i_{sp} + \frac{\delta_m U_{dc}}{L}, \quad m = 1, 2, \ldots, 40 \qquad (8)$$

Based on the solution of the standard equation in equation (7), the solution of equation (8) can be obtained, as shown in equation (9).

$$i_{sp} = \frac{\delta_m U_{dc}}{R} + C_m e^{-\frac{R}{L}t}, \quad m = 1, 2, \ldots, 40 \qquad (9)$$

Let the initial state of current be i_n, the system experiences the forty states of equation (7) in sequence according to the proposed method, and let the time for each state to take effect be $t_j, j = 1, 2, \ldots 40$, thereby solving the final state of the current i_{n+1} at the end of a switching period T_s.

When the system goes through the first state, m in equation (9) is equal to 1, the variation of the current is determined by the differential equation:

$$\frac{di_{sp}}{dt} = -\frac{R}{L}i_{sp} + \frac{\delta_1 U_{dc}}{L} \qquad (10)$$

and the current value at the end of the state is its solution.

$$i_{sp}\big|_{t=t_1} = \frac{\delta_1 U_{dc}}{R} + C_1 e^{-\frac{R}{L}t}. \qquad (11)$$

According to the initial condition

$$i_{sp}\big|_{t=0} = i_n = \frac{\delta_1 U_{dc}}{R} + C_1, \qquad (12)$$

The coefficient that can be solved as:

$$C_1 = i_n - \frac{\delta_1 U_{dc}}{R}. \qquad (13)$$

When the system is subjected to the forty state, m in equation (9) is equal to 40, the variation of the current is based on the differential equation:

$$\frac{di_{sp}}{dt} = -\frac{R}{L}i_{sp} + \frac{\delta_{40} U_{dc}}{L} \qquad (14)$$

and the current value at the end of the state is:

$$i_{sp}\big|_{t=\sum_{j=1}^{40} t_j} = \frac{\delta_{40} U_{dc}}{R} + C_{40} e^{-\frac{R}{L}t}. \qquad (15)$$

the coefficient C_{40} of the fortieth differential equation can be determined as:

$$
\begin{aligned}
C_{40} &= \frac{(\delta_{39} - \delta_{40})U_{dc}}{R} e^{\frac{R}{L}\sum_{j=1}^{39} d_j T_s} + C_{39} \\
&= \frac{(\delta_{39} - \delta_{40})U_{dc}}{R} e^{\frac{R}{L}\sum_{j=1}^{39} d_j T_s} \\
&\quad + \frac{(\delta_{38} - \delta_{39})U_{dc}}{R} e^{\frac{R}{L}\sum_{j=1}^{38} d_j T_s} \\
&\quad + \frac{(\delta_{37} - \delta_{38})U_{dc}}{R} e^{\frac{R}{L}\sum_{j=1}^{37} d_j T_s} \\
&\quad + \frac{(\delta_{36} - \delta_{37})U_{dc}}{R} e^{\frac{R}{L}\sum_{j=1}^{36} d_j T_s} \\
&\quad + \ldots \\
&\quad + \frac{(\delta_{3} - \delta_{4})U_{dc}}{R} e^{\frac{R}{L}\sum_{j=1}^{3} d_j T_s} \\
&\quad + \frac{(\delta_{2} - \delta_{3})U_{dc}}{R} e^{\frac{R}{L}\sum_{j=1}^{2} d_j T_s} \\
&\quad + \frac{(\delta_{1} - \delta_{2})U_{dc}}{R} e^{\frac{R}{L}d_1 T_s} + \left(i_n - \frac{\delta_1 U_{dc}}{R}\right) \qquad (16)
\end{aligned}
$$

namely,

$$C_{40} = \sum_{k=1}^{39} \left[\frac{(\delta_k - \delta_{k+1})U_{dc}}{R} e^{\frac{R}{L}\sum_{j=1}^{k} d_j T_s} \right] + \left(i_n - \frac{\delta_1 U_{dc}}{R}\right) \qquad (17)$$

Therefore, after going through the forty state, the current value is,

$$i_{sp}\big|_{t=\sum_{j=1}^{40} t_j} = \frac{\delta_{40} U_{dc}}{R} + C_{40} e^{-\frac{R}{L}t}, \qquad (18)$$

that is,

$$
\begin{aligned}
i_{n+1,sp} &= \frac{\delta_{40} U_{dc}}{R} + \left(i_{n,sp} - \frac{\delta_1 U_{dc}}{R}\right) e^{-\frac{R}{L}T_s} \\
&\quad + \left\{ \sum_{k=1}^{39} \left[\frac{(\delta_k - \delta_{k+1})E}{R} e^{\frac{R}{L}\sum_{j=1}^{k} d_j T_s} \right] \right\} e^{-\frac{R}{L}T_s} \qquad (19)
\end{aligned}
$$

This is the discrete model of the 21-level MMC.

IV. STEADY STATE CALCULATION

The extended PR controller is to add a time-delayed feedback control to the traditional controller. It has a higher proportional gain than ordinary PR controllers, and is able to improve the response speed of the system [18]. The transfer function of traditional PR controllers is shown in equation (20).

$$F(s) = K_p + \frac{K_r \cdot s}{s^2 + \omega_1^2} \qquad (20)$$

where K_p is the proportional gain, K_r is the resonance gain, and ω_1 is the resonance frequency. Equation (20) can be expressed in the form of discrete domain by backward differentiation method, as shown in equation (21).

$$y(n) = K_p x(n) + \frac{1}{T_s^2 \omega_1^2 + 1} \big[T_s K_r (x(n) - x(n-1))$$
$$+ 2y(n-1) - y(n-2) \big] \quad (21)$$

where, T_s is the step length of PR controller discretization. In order to eliminate the influence of unstable periodic orbits, a time-delayed feedback controller is added, as shown in equation (22).

$$f_{Dn} = \eta(i_{n,sp} - i_{n+1,sp}) \quad (22)$$

Therefore, the extended PR controller can be expressed as follows:

$$f_n = f_{P_n} + f_{R_n} + f_{D_n} \quad (23)$$

where f_n is the output of the extended PR controller, f_{Pn}, f_{Rn} and f_{Dn} are the proportion term, resonance term and time delay term, respectively, and their values are:

$$f_{Pn} = K_p(I_{ref} - i_{n,sp}) \quad (24)$$
$$f_{R_n} = \frac{1}{T_s^2 \omega_1^2 + 1} \Big\{ \{ T_s K_r \big[(I_{ref} - i_{n,sp}) - (I_{ref} - i_{n-1,sp}) \big]$$
$$+ 2f_{R_{n-1}} - f_{R_{n-2}} \} \Big\} \quad (25)$$
$$f_{D_n} = \eta(i_{n,sp} - i_{n-1,sp}) \quad (26)$$

where I_{ref} is a given value of the current.

The discrete mode of the 21-level MMC is composed of equations (19) and (23), and the whole system are a 12-order model, in which PR controller accounts for nine orders and load current accounts for three orders. It can be seen that the extended delay link does not increase the total order of the system, and both the extended PR controller and the traditional PR controller are of three orders each phase. In terms of this 12-order model, four new variables are defined as follows:

$$x_n = f_{R_{n-2}}, \quad y_n = f_{R_{n-1}}, \quad z_n = i_{n-1,sp}, \quad q_n = i_{n,sp} \quad (27)$$

A new 12-order discrete model can be obtained by substituting equation (27) into equations (19) and (23), as shown in equation (28).

$$\begin{cases} x_{n+1} = y_n, \\ y_{n+1} = \xi_1 x_n + \xi_2 y_n + \xi_3 z_n + \xi_4 q_n, \\ z_{n+1} = q_n, \\ q_{n+1} = \frac{\delta_{40} U_{dc}}{R} + \left(q_n - \frac{\delta_1 U_{dc}}{R} \right) e^{-\frac{R}{L} T_s} \\ \qquad + \left\{ \sum_{k=1}^{39} \left[\frac{(\delta_k - \delta_{k+1}) U_{dc}}{R} e^{\frac{R}{L} \sum_{j=1}^{k} d_j T_s} \right] \right\} e^{-\frac{R}{L} T_s} \end{cases}$$

TABLE 1. Parameters of MMC-HVDC for Wind Farm Integration.

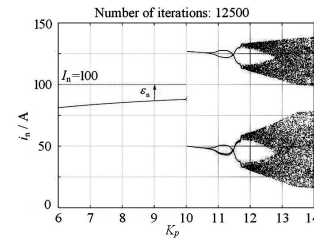| Parameters	U_{dc}	R	L	F_s	f_1
Values	160 kV	10 Ω	30 mH	10 kHz	20 Hz

FIGURE 4. Bifurcation diagram with proportional gain K_p ($K_r = 0$ and $\eta = 0$).

where, $\xi_1 = \frac{-1}{T_s^2 \omega_1^2 + 1}, \xi_2 = \frac{2}{T_s^2 \omega_1^2 + 1}, \xi_3 = \frac{T_s K_r}{T_s^2 \omega_1^2 + 1}, \xi_4 = \frac{-T_s K_r}{T_s^2 \omega_1^2 + 1}.$

V. BIFURCATION AND CHAOS ANALYSIS

The simulation model is built according to Fig. 2, and the simulation parameters are shown in Table 1. Where U_{dc} is the DC source voltage, R and L are the load resistance and inductance, F_s is the switching frequency, and f_1 is the given current frequency. The basic parameters of all bifurcation diagrams in this chapter is shown in Table 1 except for special instructions.

Firstly, an oscillation with an AC oscillation frequency of about 20 Hz is simulated, and the influence of controller parameter selection on system stability is studied through the system bifurcation chaos.. When the parameters of the extended PR controller change, the bifurcation phenomenon of the load current is shown in Fig. 4 to Fig. 6. Each frame is the result of 12500 iterations of the state equation, and the ordinate in the figure is the sampling value of the load current in the wave crest. As shown in this figure, an one-dimensional bifurcation diagrams requires two layers of loops for the state equation. The inner loop is to get the current temporal waveform with a specific bifurcation parameter K_p, and the outer loop is to sample the different current temporal waveform obtained by different bifurcation parameter K_p to get the peak value of load current. Taking the bifurcation parameters and the peak value of load current as the coordinate axes, the one-dimensional bifurcation diagram of load current is obtained.

As shown in Fig. 4, when the parameters $K_r = 0$ and $\eta = 0$, that is, only in the case of proportional control, the load current remains stable when $K_p < 10$, and the period doubling bifurcation occurs when $K_p = 10$. Because of sampling at the given peak of sinusoidal current and considering the static difference of the proportional controller, the current value in and the current peak $I_n = 100$ differ by. When $K_p = 10.8$, the load current exhibits phenomena of the fourth period. As K_p continues to increase, when $K_p > 11.8$, the load current tends to be chaotic and random.

By adjusting the parameters of the program, Fig. 5 shows the current bifurcations at different resonance gains. When
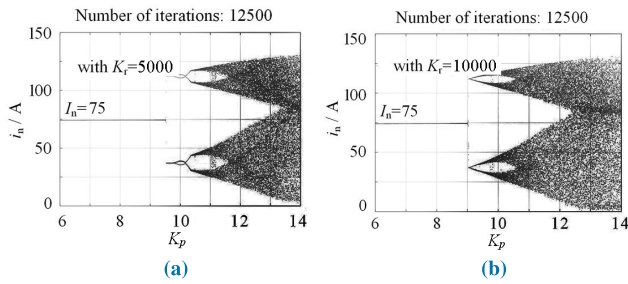
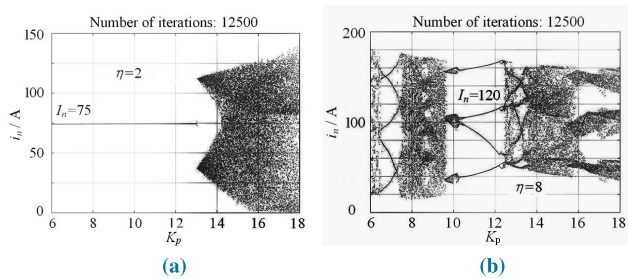**FIGURE 5.** Bifurcation diagram with different parameters K_r ($\eta = 0$).

FIGURE 6. Current bifurcation diagram with different parameters.

(a) view a **(b)** view b **(c)** view c

FIGURE 7. Shape of load current in the $K_p - K_r - \eta$ phase space of the stable domain.

(a) **(b)**

FIGURE 8. Bifurcation diagram with proportional controller.

$K_r = 5000$, the bifurcation point of the current is $K_p = 9.5$; when $K_r = 10000$, the bifurcation point of the current moves to the left, the maximum proportional gain decreases, and the bifurcation occurs at $K_p = 9$. It indicates that in order to maintain stability of the system, the resonance gain is inversely proportional to the maximum value of the proportional gain.

To observe the influence of the time-delayed coefficient on the current stability, the current bifurcation diagram with time-delayed coefficients of $\eta = 2$ and $\eta = 8$ is shown in Fig. 6. When the time-delayed coefficient $\eta = 2$, the bifurcation point of current is $K_p = 13$. Compare with Fig. 4, the bifurcation point of current is at $K_p = 10$ when the time-delayed control is not added, which also shows that the addition of a time-delayed controller may increase the maximum proportional gain of the PR controller. However, the loads current suddenly becomes chaotic when the time-delayed coefficient is too large, for example $\eta = 8$, which indicates that there is an upper limit for the time-delayed coefficient, and only within this upper limit will the load current remain stable.

By using the MATLAB solution, we can get the three-dimensional stable region of the load current in the phase space $K_r - K_p - \eta$, as shown in Fig. 7. Figs. 7a, 7b and 7c are the same graphic model from different perspectives, which can be obtained with the view () function in Matlab. In the view (az, el) function, parameter az represents the angle between the visual angle and the y-axis; parameter el indicates the angle between the visual angle and the z-axis, and both their units are degree. It should be noted that the colors in the figure have no statistical meaning, but just to show the surface of the three-dimensional area
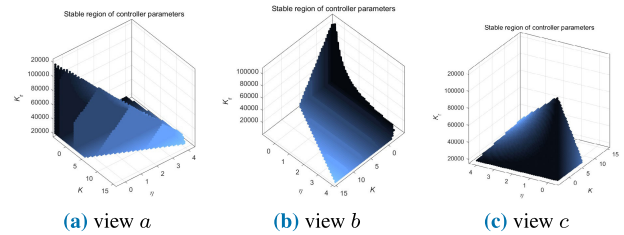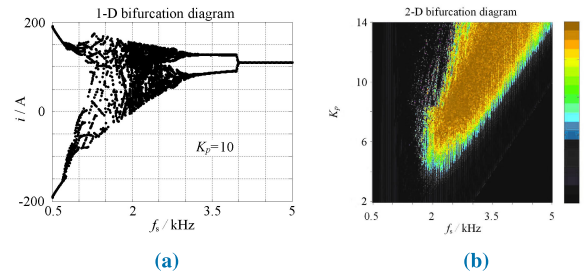
more clearly. It is easy to determine whether a coordinate points to belong to this area with the application of the data cursor function of the drawing window in Matlab, and this area of approximate vertebral body shows the value range of controller parameters more intuitively.

VI. NUMERICAL ANALYSIS

For the bifurcation and chaos analysis of the MMC, the parameters shown in Table 1 are selected for the experiment. For compariation, the system firstly only added the proportional controller with $K_p = 10$. For the grid-side current, the current is sampled at its peak time, and the sampling points at different switching frequencies can be got.

The one-dimensional bifurcation diagram of the current changing with the switching frequency is obtained. As shown in Fig. 8a, when the switching frequency $F_s > 4$ kHz, the current is in the stable state. When the switching frequency $F_s < 4$ kHz, the current is no longer stable and transits into the bifurcation state. As the switching frequency continues to decrease, the current enters the chaos state and no longer follows the obvious rule. When the sampling frequency is about 2 kHz, the current randomness is the most obvious. When the switching frequency F_s drops below 1 kHz, the MMC-HVDC cannot work. Its output current is square wave with the same cycle and switching frequency, and gradually approaches two fixed values.

The two-dimensional bifurcation diagram under proportional control is given by simulation. As shown in Fig. 8b, the blue area represents stable state, and the yellow area represents chaos state. It can be seen that the stable state is located in the blue triangle area in the right corner.

The stability of the current is observed by changing the coefficient of the time-delay controller. When $K_p = 10$,
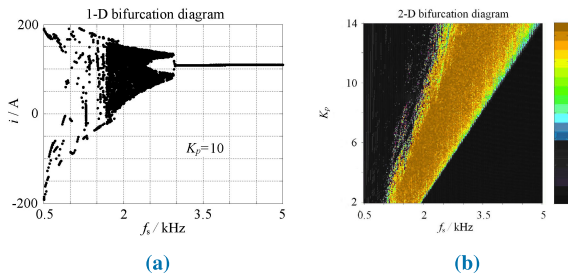
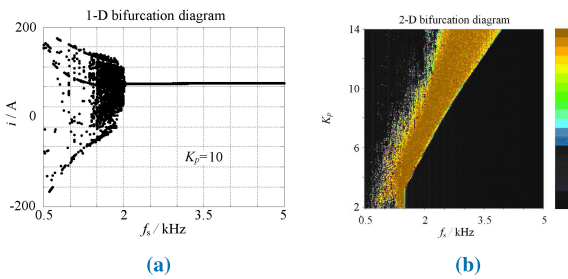**FIGURE 9.** Bifurcation diagram with TDFC when $\eta = 2$.

FIGURE 10. Bifurcation diagram with TDFC when $\eta = 6$.

$\eta = 2$, the bifurcation diagram of current changing with switching frequency is shown in Fig. 9a. Compared with Fig. 8a, the proportional controller is out of stable state when the switching frequency $F_s < 4$ kHz, while the system with TDFC control begins to become unstable when the switching frequency is $F_s < 3$ kHz. It is shown that the TDFC controller can effectively enhance the stability of the system in the middle and low frequency. Fig. 9b shows the two-dimensional bifurcation when the delay coefficient $\eta = 2$. Compared with Fig. 8b, it can be seen that the range of the blue triangle stability area in the right corner is greatly increased.

When $K_p = 10$, $\eta = 6$, the one-dimensional bifurcation diagram of the current is shown in Fig. 10a. When the switching frequency $F_s < 2$ kHz, the system begins to enter the unstable state. The two-dimensional bifurcation diagram is shown in Fig 10b. Compared with Fig. 9b, it can be seen that when the coefficient $\eta = 4$, the system can maintain stability in a large area at the right corner. Simulation results show that when the controller parameters are $K_p = 10$, $\eta = 4$, the current begins to appear instability at the switching frequency $F_s = 1.5$ kHz.

In order to observe the bifurcation and chaos of MMC-HVDC under different switching frequencies, the simulation is made and TDFC is used to control the chaos. The selected parameters are $K_p = 8, K_r = 10000, \eta = 0, F_s = 3$ kHz. Take the current sampling points at each nT_s time to draw a stroboscopic sampling diagram, as shown the red dot in Fig. 11. It is shown that when the current is in the stable state, its stroboscopic sampling diagram is a regular sine line. The black line in Fig. 11 is a time domain waveform obtained by sampling current at the interval of sampling period $T_s = 20$ ms. The graph is a straight line connecting
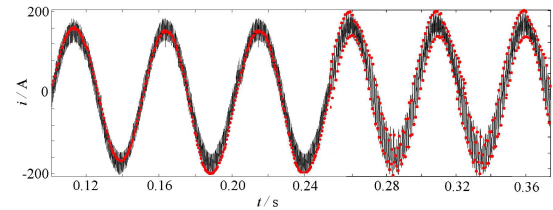

FIGURE 11. Current stroboscopic sampling diagram and the time domain waveforms with different switching frequencies.
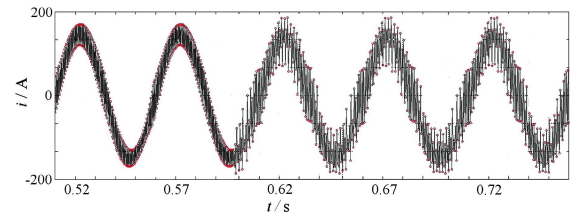

FIGURE 12. Current stroboscopic sampling diagram and the time domain waveforms with different switching frequencies.
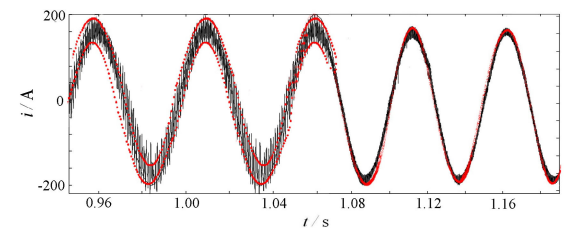

FIGURE 13. Current stroboscopic sampling diagram and the time-domain waveforms with TDFC controller.

each sampling current point, which mainly describes the current change of two adjacent sampling points.

When the switching frequency is reduced to $F_s = 2$ kHz at $t = 0.25$ s, the current is in the critical point of bifurcation state. At this time, the current stroboscopic sampling diagram is composed of two sinusoids, as shown in Fig. 11. The current time domain diagram shows the current fluctuation between two sinusoids.

When the switching frequency continues to decrease to $F_s = 1$ kHz at $t = 0.58$ s, the current stroboscopic sampling diagram and the current time-domain waveforms are shown in Fig. 12. The current is already in a chaos state. From the stroboscopic sampling diagram, at this time, the sine wave no longer has an obvious rule to follow, and the value at each peak is almost random.

When the switching frequency is got to $F_s = 2$ kHz, the current time-domain waveforms and the current stroboscopic sampling diagram are shown in Fig. 13, and the current is in the bifurcation state. After adding TDFC control at time $t = 1.07$ s with the parameters $K_p = 8, K_r = 10000, \eta = 6$, the current transits from the bifurcation state to the stable state.

In general, this experiment verifies the suppression effect of the proposed TDFC controller on bifurcation of the current
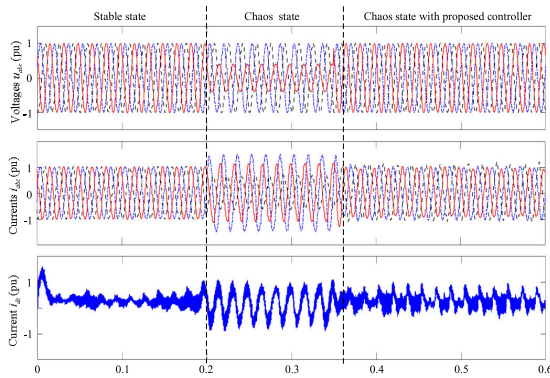
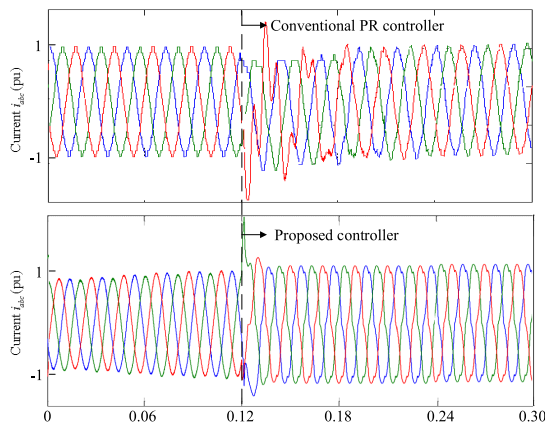**FIGURE 14.** Control effect of proposed method for oscillation current.

FIGURE 15. Control effect of the conventional PR controller and the proposed controller.
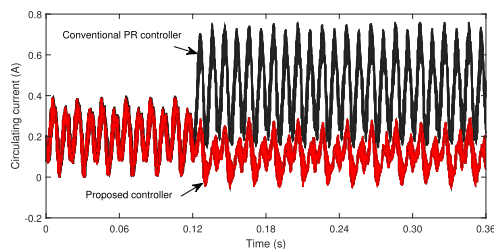

FIGURE 16. Circulating current fault at t=0.12s.

through observing the rapid changes of the current from stable to chaos. Experimental comparisons have been performed at different switching frequencies, indicating that the higher the switching frequency, the larger the stability interval of the proportional gain, which is in accordance with the result of theoretical calculation.

Fig. 14 shows the comparison of simulation results before and after using the current suppression strategy of oscillation proposed in this paper. It can be seen from Fig. 14 that when the proposed method is not adopted, the input current of MMC has obvious oscillation, and the oscillation frequency is about 20 Hz, close to equal amplitude oscillation. It can be seen from Fig. 14 that the input oscillation current of

MMC is significantly suppressed by adopting the proposed method, thus verifying the correctness and effectiveness of the proposed oscillation current suppression strategy.

The control effect of the controller is verified by simulation of power grid fault. Two groups simulation with and without TDFC control are simulated respectively. The power grid fails in t = 0.12s. Adding the conventional PR controller and the proposed controller, the grid current waveform before and after the fault is obtained as shown in Fig. 15. The circulating current is shown in Fig. 16. It can be seen that the error of compensation current is smaller than that of command current after adding TDFC control, which shows that the compensation performance of proposed controller is better than the traditional PR controller.

VII. CONCLUSIONS
In this paper, a traversing method is proposed and has successfully solved the problem of discrete modeling on multi-level converters, and provides a discrete mapping model of 21-level MMC-HVDC for wind farm integration. With this model, this paper has conducted research on the bifurcation and chaos of the load current under different control parameters and determine the stability interval of the current in the phase space $K_p - K_r - \eta$. Through the adoption of the extended PR controller and the addition of the time-delay link, the upper limit of the proportional gain is effectively improved, which plays an important role in optimizing the current loop. From the point of view of converter station control, the oscillation current output from the wind farm is obviously suppressed by adding the proposed method to the control system of the sending-end converter station.

The nonlinear dynamic behavior will seriously affect the stability of the power electronic converter. It will reduce the working life of the converter, and even lead to the sudden collapse of the connected power grid. Therefore, it is not enough to analyze all kinds of nonlinear dynamic behaviors in the converter, but also to consider the model uncertainties and external disturbances [19]. The effective measures, for example, sliding mode control [20], can be taken to control the complex behaviors of the system. The stable operation domain of the system parameter will be expanded to improve the stability performance and ensure the safe operation of the converter in a stable state.

REFERENCES
[1] N.-T. Quach, S. H. Chae, S.-H. Song, and E.-H. Kim, "Frequency and voltage control strategies of the Jeju Island power system based on MMC-HVDC systems," *J. Power Electron.*, vol. 18, no. 1, pp. 204–211, 2018.

[2] J. Zhang and C. Zhao, "Control strategy of MMC-HVDC under unbalanced grid voltage conditions," *J. Power Electron.*, vol. 15, no. 6, pp. 1499–1507, Nov. 2015.

[3] D. Ramirez, F. Martinez-Rodrigo, S. de Pablo, and L. C. H.-de Lucas, "Assessment of a non linear current control technique applied to MMC-HVDC during grid disturbances," *Renew. Energy*, vol. 101, pp. 945–963, Feb. 2017.

[4] L. Cai, U. Karaagac, and J. Mahseredjian, "Simulation of startup sequence of an offshore wind farm with MMC-HVDC grid connection," *IEEE Trans. Power Del.*, vol. 32, no. 2, pp. 638–646, Apr. 2017.

[5] J. Lyu, X. Cai, and M. Molinas, "Optimal design of controller parameters for improving the stability of MMC-HVDC for wind farm integration," *IEEE J. Emerg. Sel. Topics Power Electron.*, vol. 6, no. 1, pp. 40–53, Mar. 2018.

[6] J. Lee, Y. Yoo, M. Yoon, and G. Jang, "Advanced fault ride-through strategy by an MMC HVDC transmission for off-shore wind farm inter-connection," *Appl. Sci.*, vol. 9, no. 12, p. 2522, Jun. 2019.

[7] M. Amin, A. Ardal, and M. Molinas, "Self-synchronization of wind farm in an MMC-based HVDC system: A stability investigation," *IEEE Trans. Energy Convers.*, vol. 32, no. 2, pp. 458–470, Jun. 2017.

[8] I. Vieto and J. Sun, "Sequence impedance modeling and analysis of type-III wind turbines," *IEEE Trans. Energy Convers.*, vol. 33, no. 2, pp. 537–545, Jun. 2018.

[9] G. Li, H. Yue, M. Zhou, and J. Wei, "Probabilistic assessment of oscillatory stability margin of power systems incorporating wind farms," *Int. J. Elect. Power Energy Syst.*, vol. 58, pp. 47–56, Jun. 2014.

[10] C. Zhang, J. Wang, J. Huang, and P. Cao, "Detection and classification of short-circuit faults in distribution networks based on fortescue approach and softmax regression," *Int. J. Elect. Power Energy Syst.*, vol. 118, Jun. 2020, Art. no. 105812.

[11] W. Sima, Z. Fu, M. Yang, T. Yuan, P. Sun, X. Han, and Y. Si, "A novel active mechanical HVDC breaker with consecutive interruption capability for fault clearances in MMC-HVDC systems," *IEEE Trans. Ind. Electron.*, vol. 66, no. 9, pp. 6979–6989, Sep. 2019.

[12] J.-W. Moon, J.-S. Gwon, J.-W. Park, D.-W. Kang, and J.-M. Kim, "Model predictive control with a reduced number of considered states in a modular multilevel converter for HVDC system," *IEEE Trans. Power Del.*, vol. 30, no. 2, pp. 608–617, Apr. 2015.

[13] J. Wang, J. Liang, C. Wang, and X. Dong, "Circulating current suppression for MMC-HVDC under unbalanced grid conditions," *IEEE Trans. Ind. Appl.*, vol. 53, no. 4, pp. 3250–3259, Jul. 2017.

[14] G. J. Li, T. T. Lie, G. B. Shrestha, and K. L. Lo, "Implementation of coordinated multiple facts controllers for damping oscillations," *Int. J. Elect. Power Energy Syst.*, vol. 22, no. 2, pp. 79–92, Feb. 2000.

[15] C. Guo, Z. Yang, L. Ning, and C. Zhao, "A novel coordinated control approach for commutation failure mitigation in hybrid parallel-HVDC system with MMC-HVDC and LCC-HVDC," *Electr. Power Compon. Syst.*, vol. 45, no. 16, pp. 1773–1782, Oct. 2017.

[16] J. Xu, C. Zhao, Y. Xiong, C. Li, Y. Ji, and T. An, "Optimal design of MMC levels for electromagnetic transient studies of MMC-HVDC," *IEEE Trans. Power Del.*, vol. 31, no. 4, pp. 1663–1672, Aug. 2016.

[17] B. Kanna and S. N. Singh, "Towards reactive power dispatch within a wind farm using hybrid PSO," *Int. J. Elect. Power Energy Syst.*, vol. 69, pp. 232–240, Jul. 2015.

[18] M. H. Khooban, A. Alfi, and D. N. M. Abadi, "Control of a class of non-linear uncertain chaotic systems via an optimal type-2 fuzzy proportional integral derivative controller," *IET Sci., Meas. Technol.*, vol. 7, no. 1, pp. 50–58, Jan. 2013.

[19] Y. Wang, B. Jiang, Z.-G. Wu, S. Xie, and Y. Peng, "Adaptive sliding mode fault-tolerant fuzzy tracking control with application to unmanned marine vehicles," *IEEE Trans. Syst., Man, Cybern. Syst.*, early access, Jan. 24, 2020, doi: 10.1109/TSMC.2020.2964808.

[20] Y. Wang, H. Shen, H. R. Karimi, and D. Duan, "Dissipativity-based fuzzy integral sliding mode control of continuous-time T-S fuzzy systems," *IEEE Trans. Fuzzy Syst.*, vol. 26, no. 3, pp. 1164–1176, Jun. 2018.

• • •